International Journal of Solids and Structures 50 (2013) 4258–4269

Contents lists available at ScienceDirect

International Journal of Solids and Structures

journal homepage: www.elsevier.com/locate/ijsolstr

Tension–torsion fracture experiments – Part II: Simulations with the extended Gurson model and a ductile fracture criterion based on plastic strain

Zhenyu Xue [a], Jonas Faleskog [b], John W. Hutchinson [c,*]

[a] Jet Research Center, Halliburton Energy Services, 8432 S. 135-W, Alvarado, TX 76009, USA
[b] Department of Solid Mechanics, Royal Institute of Technology, SE-100 44 Stockholm, Sweden
[c] School of Engineering and Applied Sciences, Harvard University, Cambridge, MA 02138, USA

ARTICLE INFO

Article history:
Received 12 October 2012
Received in revised form 15 August 2013
Available online 3 September 2013

Keywords:
Ductile fracture
Fracture in shear
Tension–torsion test
Fracture criterion
Lode parameter

ABSTRACT

An extension of the Gurson model that incorporates damage development in shear is used to simulate the tension–torsion test fracture data presented in Faleskog and Barsoum (2013) (Part I) for two steels, Weldox 420 and 960. Two parameters characterize damage in the constitutive model: the effective void volume fraction and a shear damage coefficient. For each of the steels, the initial effective void volume fraction is calibrated against data for fracture of notched round tensile bars and the shear damage coefficient is calibrated against fracture in shear. The calibrated constitutive model reproduces the full range of data in the tension–torsion tests thereby providing a convincing demonstration of the effectiveness of the extended Gurson model. The model reinforces the experiments by highlighting that for ductile alloys the effective plastic strain at fracture cannot be based solely on stress triaxiality. For nominally isotropic alloys, a ductile fracture criterion is proposed for engineering purposes that depends on stress triaxiality and a second stress invariant that discriminates between axisymmetric stressing and shear dominated stressing.

1. Introduction

Trends in fracture ranging from zero to relatively high stress triaxiality brought out in Faleskog and Barsoum (2013) (hereafter designated as Part I) for two steels, Weldox 420 and 960, reveal that the effective plastic strain at fracture is not monotonically related to stress triaxiality. This trend was first highlighted earlier in a series of fracture tests by Bao and Wierzbicki (2004) on Al 2024-T351. Moreover, the Bao–Wierzbicki experiments demonstrated that some metal alloys have less ductility under pure shear than under axisymmetric stress states with significantly higher triaxiality. These experimental findings have motivated recent efforts to extend damage-based constitutive models such as the Gurson model (1977) to more realistically predict fracture under low stress triaxiality conditions including pure shear (Nahshon and Hutchinson, 2008; Xue and Wierzbicki, 2008). In this paper, designated as Part II, the extended Gurson model will be employed to simulate the tension–torsion tests of the two steels presented in Part I. Guided by the experimental data and predictions of the extended Gurson model, a modification of the stress-dependence of the critical effective plastic strain will be proposed for a widely used ductile fracture criterion (Hancock and Mackenzie, 1976; Johnson and Cook, 1985).

The distinction between *axisymmetric stress states* and *shearing states* plays an important role in the fracture trends noted above. Denote the stress by σ_{ij}, the mean stress by $\sigma_m = \sigma_{kk}/3$, the stress deviator by $s_{ij} = \sigma_{ij} - \sigma_m\delta_{ij}$, and the effective stress by $\sigma_e = \sqrt{3s_{ij}s_{ij}/2}$. Denote the ordered principal stresses by $\sigma_I \geqslant \sigma_{II} \geqslant \sigma_{III}$. In addition to σ_m and σ_e, two other related measures of the stress state will be useful in characterizing the fracture trends confronted in this paper: the Lode parameter,

$$L = \frac{2\sigma_{II} - \sigma_I - \sigma_{III}}{\sigma_I - \sigma_{III}}, \tag{1}$$

and the ω -measure introduced by Nahshon and Hutchinson,

$$\omega(\boldsymbol{\sigma}) = 1 - \left(\frac{27J_3}{2\sigma_e^3}\right)^2, \tag{2}$$

with

$$J_3 = \det(\mathbf{s}) = s_{ij}s_{ik}s_{kj}/3 = (\sigma_I - \sigma_m)(\sigma_{II} - \sigma_m)(\sigma_{III} - \sigma_m).$$

The Lode parameter lies in the range, $-1 \leqslant L \leqslant 1$, while the ω has the range $0 \leqslant \omega \leqslant 1$; they are related by

* Corresponding author. Tel.: +1 617 495 2848; fax: +1 617 495 9837.
E-mail address: hutchinson@husm.harvard.edu (J.W. Hutchinson).

0020-7683/$ - see front matter © 2013 Elsevier Ltd. All rights reserved.
http://dx.doi.org/10.1016/j.ijsolstr.2013.08.028

$$\omega = \frac{27(L^2-1)^2}{(3+L^2)^3}. \tag{3}$$

Both measures discriminate between axisymmetric and shearing stress states, as will now be discussed.

Axisymmetric stress states are characterized by either

$$\text{Case I}: \quad \sigma_I \geqslant \sigma_{II} = \sigma_{III} \quad (\omega = 0,\ L = -1), \text{or} \tag{4}$$

$$\text{Case II}: \quad \sigma_I = \sigma_{II} \geqslant \sigma_{III} \quad (\omega = 0,\ L = +1). \tag{5}$$

The ω -measure is zero for all axisymmetric stress states. The magnitude of the Lode parameter is unity for these states, but it discriminates between a uniaxial stress plus a hydrostatic component (Case I in (4) with $L = -1$) and an equi-biaxial stress state plus a hydrostatic component (Case II in (5) with $L = 1$). In this paper, for lack of better terminology, states comprised of a pure shear stress, $\tau > 0$, plus a hydrostatic component, σ_m,

$$\sigma_I = \tau + \sigma_m, \quad \sigma_{II} = \sigma_m, \quad \sigma_{III} = -\tau + \sigma_m \qquad (\omega = 1,\ L = 0) \tag{6}$$

are referred to as *shearing stress states*. For all such states, $\omega = 1$ and $L = 0$.

The original formulation of the Gurson model does not account for damage growth and material softening in pure shear unless continuous void nucleation occurs. The original version predicts that fracture does not occur at zero triaxiality under pure shear. The only fundamental change to the Gurson model in the extension of Nahshon and Hutchinson (2008) is the modification of the equation governing the increment of damage growth $\dot{f}$:

$$\dot{f} = (1-f)\dot{\varepsilon}^p_{kk} + k_\omega f \omega(\boldsymbol{\sigma}) \frac{s_{ij}\dot{\varepsilon}^p_{ij}}{\sigma_e} \tag{7}$$

with $\dot{\varepsilon}^p_{ij}$ as the plastic strain increment. The first contribution is that incorporated in the original model while the second is the extension. The modification deliberately leaves the constitutive relation unaltered for axisymmetric stress states ($\omega = 0$) because the Gurson model and its subsequent calibrations were based on axisymmetric void growth solutions. The effect of the modification is felt most strongly for shearing states ($\omega = 1$). In a state of pure shear stress, (7) gives $\dot{f} = k_\omega f \dot{\gamma}^p/\sqrt{3}$, where $\dot{\gamma}^p$ is the plastic shear strain rate and k_ω is the shear damage coefficient, the sole new parameter in the extended model. The inclusion of the second term in (7) rests on the notion that the volume of voids undergoing shear may not increase, but void deformation and reorientation contribute to softening and constitute an effective increase in damage. In addition, the second term can model damage generated by the shear of tiny secondary voids in void sheets linking larger voids. Thus, in the extension, f is no longer directly tied to the plastic volume change. Instead, it must be regarded either as an effective void volume fraction or simply as a damage parameter, as it is, for example, when the Gurson model is applied to materials with distinctly non-spherical voids. Recent simulations of void interaction in shear by Tvergaard (2008, 2009) and Tvergaard and Nielsen (2010) have shown that this phenomenological extension of Gurson model can capture quantitative aspects of softening and localization in shear if k_ω is properly calibrated. More generally, other recent theoretical studies (Barsoum and Faleskog, 2011; Scheyvaerts et al., 2010) have helped to clarify the role of the Lode parameter in characterizing void growth and shear localization.

The extension of Gurson model does not alter the yield function:

$$F(\sigma_e, \sigma_m, f) = \left(\frac{\sigma_e}{\sigma_M}\right)^2 + 2q_1 f \cosh\left(\frac{3q_2}{2}\frac{\sigma_m}{\sigma_M}\right) - (1 + q_3 f^2). \tag{8}$$

Here, σ_M is the flow stress of the undamaged material at the current matrix strain. This is an input to the model that has been obtained experimentally for each of the two steels in the study, as will be described. The three parameters, q_i, have been calibrated specifically for the steels in this study in the manner described by Faleskog et al. (1998) and Kim et al. (2004) with values listed later. Further discussion of the model and suggestions for its calibration are given by Nahshon and Hutchinson (2008) and Xue et al. (2010). The reader is referred to these references for a complete listing of the equations governing the constitutive model.[1] It can also be noted that the constitutive model used in carrying out the present calculations employed accelerated void grow for $f > f_C = 0.15$, as is commonly done to model final failure behavior (Xue et al., 2010). However, none of the results presented in this paper are affected by the accelerated void growth because the fracture strain as defined here is attained when f is everywhere smaller than f_C, as described later.

To provide a background to the trends seen in the experiments in Part I and in the tests of Bao and Wierzbicki (2004), a selection of localization predictions based on the Gurson model and its extension is presented in the next section. The objective of this brief "primer on localization" is to bring out the significant difference between localization under axisymmetric stressing from that under shear stressing – this difference is at the heart of the fracture trends addressed here and in Part I.

2. Basic results on localization

The localizations of interest here are localization bands (shear and normal separation bands) *not* necking localizations. Shear and normal separation localization bands have a thickness set by material microstructure, typically on the order of tens of microns. In ductile alloys, they often occur within a necking localization whose thickness is set by overall geometry, e.g., the diameter of a tensile bar or the thickness of a plate. The onset of a shear band or a normal separation band marks the maximum overall strain possible for that stress state because, once the band forms, essentially all of the subsequent deformation in the local vicinity takes place within the band; material outside the band will then usually unload elastically. The critical strain in the material outside the band at localization defines the relevant fracture strain for engineering purposes. A similar definition of fracture is adopted by Barsoum and Faleskog (2011) in their study of the combined roles T and L in localization. Their study makes use of three dimensional void growth simulations to describe behavior within the band and thereby complements the present study in that it is not tied to the Gurson model.

2.1. Stress-state dependence of shear and normal localizations

The predictions presented in this section are drawn from Nahshon and Hutchinson (2008) and from additional localization computations similar to those reported in that reference carried out in preparation of this paper. The material parameters are those for the steel Weldox 420 which will be detailed in full later in the paper. To a high degree of approximation, Weldox 420 is initially isotropic with a relatively high strain hardening index, $N = 0.18$. The calibrated values of the initial effective void volume fraction and shear damage coefficient are $f_0 = 0.005$ and $k_\omega = 1.1$, as will be detailed later.[2] Results computed with $k_\omega = 0$ are those for the conventional Gurson model; those with $k_\omega > 0$ are based on the extended model. The trends which follow for Weldox 420 are similar to those

[1] There is an error in both references in the expression for $\partial F/\partial\sigma_M$. The sign of the second term should be minus not plus.

[2] The tensile stress–strain curve characterizing the base material in this section uses a pure-power relation between plastic strain and stress and is somewhat simpler than that used in simulations in Section 3. This difference has essentially no effect on the trends presented.

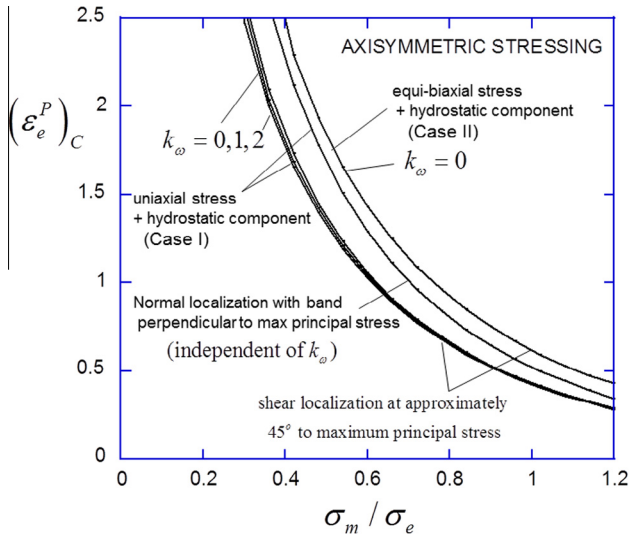

Fig. 1. Effective plastic strain at localization as a function of stress triaxiality for axisymmetric stressing as predicted by the Gurson model ($k_\omega = 0$) and its extension $k_\omega > 0$. The material properties are those of Weldox 420 given in the text. Inside the band $f_0 = 0.005$ while outside the band $f_0 = 0$. Curves are shown for Case I having stress states with uniaxial stress plus a hydrostatic component (4) and for Case II having an equi-biaxial stress state plus a hydrostatic component (5). For Case I, two sets of results are shown: *normal localizations* in which the band is restricted to be normal to the maximum principal stress such that the deformation within the band is uniaxial straining in the normal direction, and *shear localizations* with the band orientation chosen to produce the minimum effective plastic strain at the onset of localization (these lie at approximately 45° to the maximum principal stress). The normal localization is strictly independent of k_ω while the shear localizations are nearly independent of k_ω for axisymmetric stressing. Similarly, the shear localization results for Case II are essentially independent of k_ω. Normal localizations for Case II are not shown.

for the higher strength steel, Weldox 960, and they can be considered representative of many tough ductile alloys.

As described in Nahshon and Hutchinson (2008), the localization simulations are based on an infinite planar band of uniform thickness sandwiched between two semi-infinite outer blocks – similar to the plane stress simulations of Marciniak and Kuczynski (1967). For the simulations in this section, the initial effective void volume fraction in the band is taken as $f_0 = 0.005$ while the effective volume fraction outside the band is taken to be zero. There are two uniform states of stress and strain – that within the band and that outside. The localization results presented in this sub-section have all been computed by imposing proportional stressing with no material rotation outside the band. Specifically, outside the band, the principal stress axes are fixed with respect to the material and the maximum principal stress, σ_I, is increased monotonically. The other two components are increased according to $\sigma_{II} = r_{II}\sigma_I$ and $\sigma_{III} = r_{III}\sigma_I$ with r_{II} and r_{III} prescribed to be constant. All possible orientations of the band are considered. That orientation which produces localization at the lowest effective plastic strain in the outer blocks is identified as the critical orientation. Rotation of the material occurs within the band. Localization is associated with the condition that the strain rates within the band grow in an unbounded manner relative to the strain rates outside the band – in most cases this coincides with the onset of elastic unloading outside the band.

Fig. 1 presents plots of the effective plastic strain at localization as a function of stress triaxiality, σ_m/σ_e, for *axisymmetric stressing* as prescribed by (4) for Case I and by (5) for Case II. The effective plastic strain is defined by

$$\varepsilon_e^P = \int_0^t \dot{\varepsilon}_e^P dt \quad \text{with } \dot{\varepsilon}_e^P = \sqrt{2\dot{\varepsilon}_{ij}^P \dot{\varepsilon}_{ij}^P/3} \tag{9}$$

with $\dot{\varepsilon}_{ij}^P$ as the logarithmic strain rates such that ε_e^P can be regarded the logarithmic measure of the effective plastic strain. The lessons to be drawn from Fig. 1 are:

(1) For the infinite blocks of uniformly strained material, the critical plastic strain is associated with a shear band in all these cases. At localization, the band is approximately 45° to the maximum principal stress direction. The effect of the shear damage coefficient k_ω is shown for Case I and it is seen that it has essentially no effect on these predictions. Similarly, there is no effect for Case II, although this is not shown. Thus, there is essentially no distinction in the localization predictions between the original Gurson model and its extension for axisymmetric stressing. The slight difference that does exist is due to the fact that the state within the band at the onset of localization is not precisely axisymmetric stressing due to the fact that the critical band orientation is not normal to the maximum principal stress.

(2) For Case I, results are shown for normal separation localizations which have been computed by restricting the band to be normal to the maximum principal stress. At localization, the strain-rate in the band is uniaxial and oriented parallel to the maximum principal stress. A normal separation localization often occurs at the center of a neck or a notch in a round tensile bar as the beginning of cup-cone failure. It is important to note that the critical strain for normal localization is only slightly larger than that associated with shear localization. In geometries like a notched round tensile bar, the constraint on shear localization due to axial symmetry can favor the emergence of a normal localization in the central region.

(3) The Gurson model predicts some difference in the plastic strain to localization between Cases I and II, although this difference is relatively small compared to that between axisymmetric and shearing states discussed next. In revising a commonly used engineering fracture criterion in Section 4, we will ignore the difference between Cases I and II and simply use $\omega = 0$ to characterize axisymmetric stress states.

Fig. 2 compares the critical effective plastic strain for *axisymmetric stressing* ($\omega = 0$) with those for *shear stressing* (6) with $\omega = 1$. All the localizations in this figure are shear bands oriented approximately 45° to the maximum principal stress at localization with the normal in the plane of (σ_I, σ_{III}). The main conclusions are:

(1) At a given triaxiality, the original Gurson model ($k_\omega = 0$) predicts an appreciably lower localization strain under shear stressing than axisymmetric stressing. Nevertheless, at low triaxiality, e.g., $\sigma_m/\sigma_e < 0.2$, localization is effectively excluded even for shear stressing. As noted earlier, localization does not occur in pure shear ($\sigma_m/\sigma_e = 0$) according to the original Gurson model without continuous nucleation of voids.

(2) The extended model predicts a strong dependence of the localization strain on k_ω under shear stressing. With $k_\omega = 1.1$, corresponding to the calibrated value for Weldox 420, the spread between localization strains under axisymmetric stressing and shear stressing is large. In pure shear, $(\varepsilon_e^P)_C \cong 1.6$.

(3) While not shown, localization strains for stress states other than axisymmetric stressing and shear stressing with $0 < \omega < 1$, fall between those shown in Fig. 2.

These conclusions are also supported by the localization study carried out by Barsoum and Faleskog (2011) based on three dimensional simulations of void deformation within the localization band.

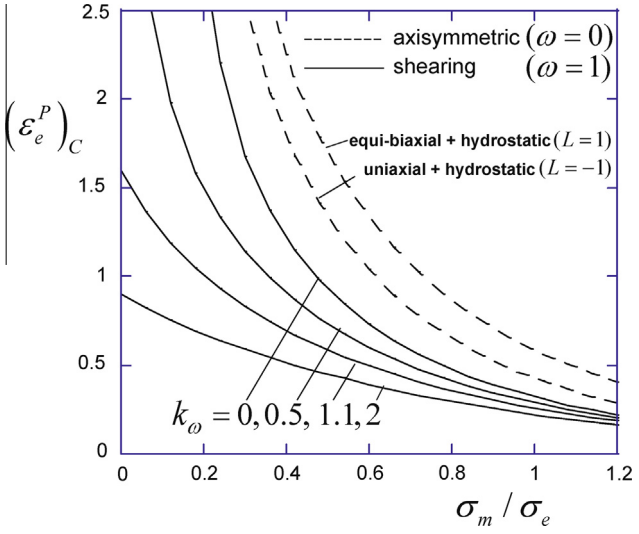

Fig. 2. Critical effective plastic strain at localization as a function of triaxiality for axisymmetric stressing and shearing stress states with $f_0 = 0.005$ inside the band. The results for axisymmetric stressing are essentially independent of the shear damage coefficient, k_ω, while those for shear stressing depend strongly on k_ω. The result for $k_\omega = 0$ is that based on the conventional Gurson model. The result for $k_\omega = 1.1$ is that based on the extended model calibrated to Weldox 420.

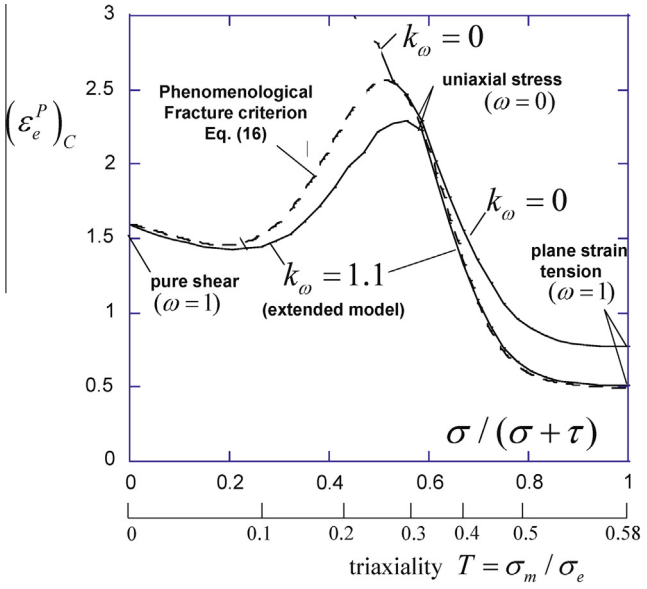

Fig. 3. Effective plastic strain at localization under proportional stressing for all combinations of shear and plane strain tension prescribed by (11). The properties of the material represented by the extended Gurson model ($k_\omega = 1.1$) are those calibrated to Weldox 420 later in the paper. The initial void volume fraction is $f_0 = 0.005$ within the localization band and $f_0 = 0$ outside the band. The predictions based on the original Gurson model ($k_\omega = 0$) and the proposed phenomenological fracture criterion in Section 4 are included for comparison.

The higher susceptibility to localization under shear stressing, compared to that under axisymmetric stressing, in large part accounts for the fact that triaxiality alone cannot capture the dependence of stress state on ductile fracture. It follows that the common practice of measuring fracture strains using axisymmetric notched tensile bars will overestimate fracture strains for non-axisymmetric stress states at corresponding levels of triaxiality.

2.2. Simplified model of the tension–torsion test

This brief primer on localization is concluded with simulations of localization for a simplified model of combined stressing in tension and shear which provide insight into the tension–torsion experiments presented in Part I.

Consider proportional stressing with $\sigma \geqslant 0$ and $\tau \geqslant 0$ in axes (x_1, x_2, x_3) with

$$\sigma_{11} = \sigma, \quad \sigma_{22} = \sigma/2, \quad \sigma_{12} = \tau, \quad \sigma_{33} = 0, \quad \sigma_{13} = 0, \quad \sigma_{23} = 0 \qquad (10)$$

such that $\sigma_m = \sigma/2$ and $\sigma_e = \sqrt{3\sigma^2/4 + 3\tau^2}$, with the ratio, τ/σ, constant in each deformation history. Because $s_{22} = 0$, $\dot{\varepsilon}^P_{22} = 0$; thus, the deformation is constrained against straining in the x_2-direction, apart from an elastic component. In principal axes of stress,

$$\sigma_I = \frac{3}{4}\sigma + \sqrt{\frac{\sigma^2}{16} + \tau^2}, \qquad (11)$$

$$\sigma_{II} = \frac{3}{4}\sigma - \sqrt{\frac{\sigma^2}{16} + \tau^2}, \quad \sigma_{III} = 0 \qquad \text{for } \tau < \sigma/\sqrt{2},$$

$$\sigma_{II} = 0, \quad \sigma_{III} = \frac{3}{4}\sigma - \sqrt{\frac{\sigma^2}{16} + \tau^2} \qquad \text{for } \tau > \sigma/\sqrt{2}.$$

The stress triaxiality and ω measure are

$$T \equiv \frac{\sigma_m}{\sigma_e} = \frac{\sigma}{\sqrt{3(\sigma^2 + 4\tau^2)}} \quad \text{and} \quad \omega = 1 - \frac{\left(6\sqrt{3}\sigma\tau^2\right)^2}{\left(\sigma^2 + 4\tau^2\right)^3}. \qquad (12)$$

The stress states specified by all combinations of (σ, τ) are similar to those in the tests of Part I in that in the two limits (pure shear, $\sigma = 0$, and plane strain tension, $\tau = 0$) are states of shear stressing with $\omega = 1$. Moreover, the intermediate state with $\tau = \sigma/\sqrt{2}$ is axisymmetric stressing with $\omega = 0$ (e.g., a uniaxial stress state with $\sigma_I = 3\sigma/2$, $\sigma_{II} = \sigma_{III} = 0$). Thus, this combination of proportional stressing histories has the same property of the tension–torsion test series in Part I in that over the range of states it evolves continuously from $\omega = 1$ when $\sigma = 0$ to an intermediate state with $\omega = 0$ and then back to $\omega = 1$ at the other limit when $\tau = 0$. Material rotation outside and within the band occurs and is accounted for in the localization simulations.

The effective plastic strain in the material outside the band at localization, $(\varepsilon^P_e)_C$, is plotted in Fig. 3 for the full range of proportional stressing histories specified by (11). Two abscissas are used: $\sigma/(\sigma + \tau)$ which varies from 0 to 1 and triaxiality in (12) which varies from 0 to 0.58, the latter corresponding to plane strain tension. A companion plot of ω is given in Fig. 4. Predictions are shown for the original Gurson model ($k_\omega = 0$) and for the extended model with $k_\omega = 1.1$. All the localizations are shear bands with normal oriented at approximately 45° to the (x_I, x_{III}) axes. The predictions of the original model and its extension are nearly coincident when $\tau = \sigma/\sqrt{2}$ because for this case the state of stress outside the band is axisymmetric with $\omega = 0$. However, for the other combinations of τ and σ significant differences between the predictions of the two constitutive models are evident. In particular, in the range of low triaxiality the original Gurson model predicts that localization will not occur, except possibly at unrealistically large strains.

The trend seen in the tension-shear simulations in Fig. 3 wherein a local maximum in the localization strain occurs at an intermediate triaxiality state corresponding (approximately) to axisymmetric stressing is qualitatively similar to the trend of tension–torsion data for fracture strains in Part I (see also Figs. 10 and 13). The range of triaxiality of the stress states in the tests in Part I is larger due to the fact that the test specimens are notched, but the non-monotonic character of the fracture strain with increasing triaxiality applies to both situations.

The tension–torsion loadings considered in this section and characterized by (10)–(12) are the same as those achieved in

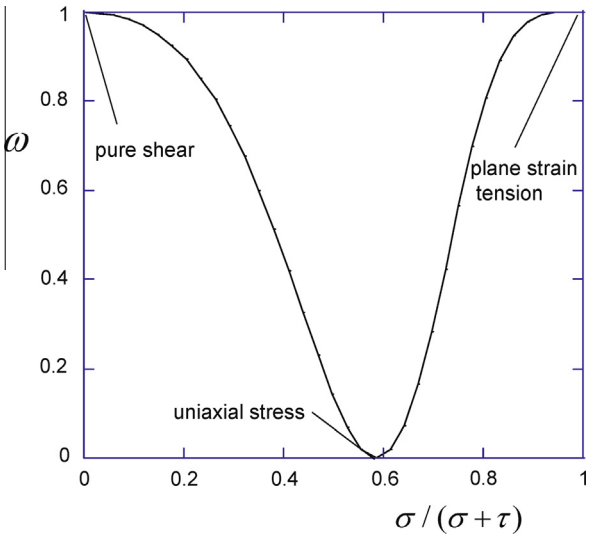

Fig. 4. The measure ω associated with the proportional stressing histories in Fig. 3.

tubular test specimens of Al 6061 designed for uniform stress and tested by Haltom et al. (2013). The critical effective plastic strains in Haltom et al., are measured within the shear localization zone. Thus, it is not possible to make direct comparison with simulations in this section which focus on the effective plastic strain just outside the localization band at the onset of localization. Unlike the trend seen in Fig. 3 and later for the two Weldox steels, the effective plastic strain reported by Haltom et al., for Al 6061 decreases monotonically with triaxiality. The range of test data achieved in the Haltom et al., test series is less than that of the simulations presented in Figs. 3 and 4 owing to plastic buckling in near-pure shear and necking of the specimen at the other limit when tension dominates.

3. Application of the extended Gurson model to simulate the tension–torsion tests of Weldox 420 and 960 and a set of notched round bar tensile tests

In this section, the procedure used to calibrate the extended Gurson model will be described and executed for the two steels, Weldox 420 and 960, reported on in Part I. Then, the extended model will be used as the constitutive module within a finite element code to simulate the full range of the tension–torsion tests on these steels allowing direct comparison with the experimental data. Experiments on a smaller set of notched round bar tensile tests will also be simulated.

3.1. Calibration of the constitutive model

Several tests are required to calibrate the extended Gurson model (Xue et al., 2010). Here, a three-step procedure has been followed: (1) data from an un-notched round bar tensile test is used to generate the tensile stress–strain curve, $\sigma(\varepsilon)$, characterizing the undamaged material; (2) data from a notched round bar tensile test is used to identify the initial void volume fraction, f_0; and (3) the pure torsion test in the series of Part I is used to calibrate k_ω. Calculations for steps (1) and (2) were carried out using the Standard version of ABAQUS (2010), while all the simulations of the tension–torsion tests, including step (3), employed the Explicit version of ABAQUS (2010). The calibration process is now described in more detail.

Considerable care has been taken to characterize the true stress-log strain tensile stress strain curve of the material in the

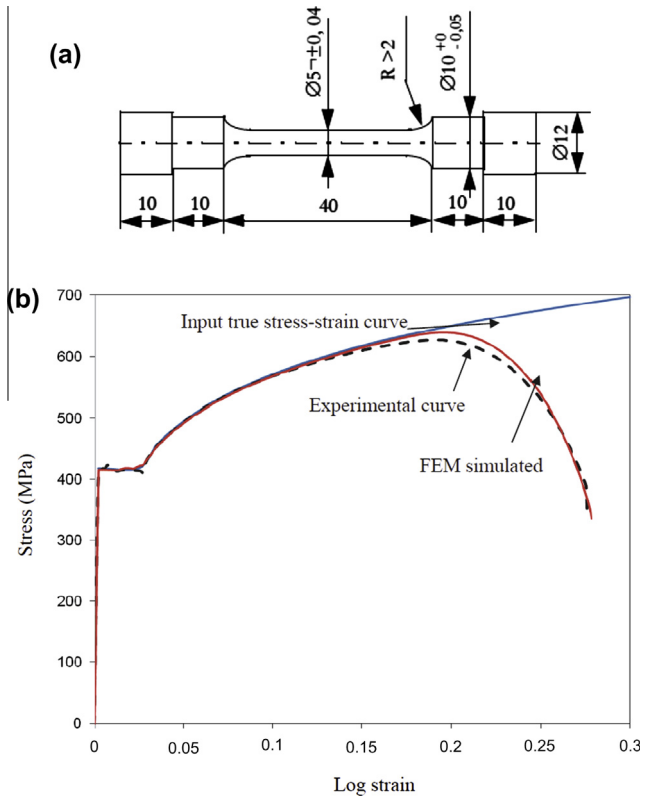

Fig. 5. (a) Dimensions of the round smooth bar specimen (in mm). (b) Stress–log strain curve for Weldox 420. For the experimental curve and FEM simulated curve, the stress plotted is determined as $(P/A_0)(L/L_0)$ where P is the load, A_0 is the initial cross-sectional area of the gage section, and L/L_0 is the ratio of deformed to undeformed length of the gage section. The log strain is $\ln(L/L_0)$. The input curve is the true stress- log strain curve (13) with parameter values given in Table 1.

absence of any damage, $\sigma(\varepsilon)$, which is the input, σ_M, in the yield function (8). This requires fitting a representation to the uniaxial data, accounting for necking, and extrapolating beyond the point where damage becomes important. With reference to the tensile data for Weldox 420 in Fig. 5, the following representation used is (see also Part I):

$$\sigma(\varepsilon) = \begin{cases} E\varepsilon & \varepsilon \leqslant \varepsilon_0 \\ \sigma_0\ (= E\varepsilon_0) & \varepsilon_0 \leqslant \varepsilon \leqslant \varepsilon_S + \varepsilon_N \\ \sigma_0\left(\frac{\varepsilon-\varepsilon_S}{\varepsilon_N}\right)^N & \varepsilon_S + \varepsilon_N \leqslant \varepsilon \end{cases} \tag{13}$$

with values of the coefficients given in Table 1. The base curve, $\sigma(\varepsilon)$, for the material with no damage is plotted in Fig. 5 showing the extrapolation to a logarithmic strain of 0.3. Included in Fig. 5 is the experimentally measured stress-overall strain curve from the smooth round bar test and the corresponding curve simulated using the finite element code employing (13) for the base material. The stress for these curves is defined as the force/current area, assuming the current area is determined as if the deformation were uniform. Similarly, the overall strain is the logarithmic strain evaluated in terms of the elongation of the gage section assuming uniform elongation. The specimen begins to neck at a strain of roughly 0.2. The abrupt downturn in the experimental curve at an overall strain of about 0.28 corresponds to the onset of a normal localization band at the center of the neck, i.e., the onset of the cup-cone failure mode. Prior to this onset, damage in the form of non-zero f_0 has relatively little effect on the simulated curve. This assertion has been verified directly and it will be illustrated below for another example. The shear damage coefficient, k_ω, and the effective void volume fraction

Table 1
Material parameters for Weldox 420 and 960. For both steels, the Young's modulus is taken as $E = 208$ GPa with Poisson's ratio, $\nu = 0.3$.

Material	σ_0 (MPa)	N	ε_0	ε_N	ε_s
Weldox 420	418	0.18	0.002	0.0162	0.0084
Weldox 960	956	0.059	0.0046	0.0046	0

at which accelerated void growth begins, f_C, have essentially no effect on the behavior of the round bar tensile test until shear-off begins in the final stages of cup-cone fracture.

The three parameters used in the yield function of the Gurson model for Weldox 420 have been taken as $q_1 = 1.07$, $q_2 = 1.01$ and $q_3 = q_1^2$ based on a separate calibration using an axisymmetric cell model subject to proportional stressing with T in the interval from 0.8 to 1.8 in a range of f_0 appropriate for the Weldox materials (Part I). The calibration process for the q's is discussed in some detail by Faleskog et al. (1998) and Kim et al. (2004). The values for Weldox 960 are $q_1 = 0.90$ and $q_2 = 1.16$.

In principle, the onset of the cup-cone failure in smooth round bar tensile test could be used to calibrate f_0, but we found that fitting to the onset of failure in a notched-round bar tensile test is more robust. The data used for the calibration is plotted in Fig. 6 as average stress versus elongation for two notched-round bar tests on Weldox 420. Two tests have been conducted for each specimen geometry. Included in this plot are curves simulating the specimen with various values of f_0. In the simulations, the onset of failure, coincident with the slope change seen in Fig. 6, is associated with the formation of a normal localization band at the center of the notch. Subsequently, the band spreads out from the center and at some stage branches as a shear band and links to the surface. Details of this failure sequence will not be reported here because they have been reported in considerable detail for similar simulations by Xue et al. (2010) where the role of the finite element mesh on the cup-cone failure mode is reported. Note that prior to the onset of failure at the slope change, the choice of f_0 has very little effect on the overall stress-elongation behavior, as mentioned earlier. At small void volume fractions representative of tough structural alloys, damage plays a critical role in giving rise to normal and shear localizations but has relatively little observable effect on overall load–deflection behavior before localization. The onset of the normal localization band is insensitive to k_ω (and f_C) in these calculations, but the transition to final shear-off depends strongly on k_ω and to a lesser extent f_C. The value $f_0 = 0.005$ has been chosen to reproduce the onset of the failure in the center of the neck associated with the slope change seen in the overall stress-elongation curves in Fig. 6. A comparison of two tests on a shallow notched bar ($a/r = 0.2$) with simulations using $f_0 = 0.005$ also show good agreement, but these are not shown.

With the base stress–strain and the initial void volume fraction in hand, the last step is to choose k_ω to fit a set of test data for which it plays an important role. For this purpose, the experimental data from pure torsion test in Part I is employed, which is included here in Fig. 7. In this case, the downturn in the experimental curve is even more abrupt. It is associated with the formation of a shear band extending across the notched region of the specimen. Based on the comparisons seen in Fig. 7, the choice $k_\omega = 1.1$ has been made. The same feature noted above with respect to the effect of f_0 on behavior prior to localization is evident in Fig. 7. That is, k_ω has a very strong influence on the shear localization strain, but its effect on overall behavior prior to localization is hardly discernable. The onset of accelerated void growth at f_C has no effect on these results because localization occurs at void volume fractions much below f_C.

Finally, a remark is in order on the accuracy of the simulations of steeply dropping load–deflection behavior seen following the onset of localization when the band extends across the loaded cross-section in Figs. 6 and 7. In the simulations, the predicted steepness of the load–deflection curve depends on element size because the band localizes to a width of essentially one element. No attempt has been made to calibrate the element size to accurately represent behavior in the post-localization regime. Thus the results following localization presented in Figs. 6 and 7 are included only to illustrate the dramatic transition following localization. These remarks also apply to the simulations of the tension–torsion experiments in the next section. The important point to note is that the emphasis in this paper is on the onset of localization at the point where the material abruptly loses its load carrying capacity and not on the behavior in the post-localization regime. The onset of localization is accurately predicted.

In summary, for Weldox 420, the base stress–strain behavior of the undamaged material is specified by (13) with parameter values listed in Table 1. The two damage-related parameters associated with the extended Gurson model are $f_0 = 0.005$ and $k_\omega = 1.1$. The calibration procedure described above was repeated for Weldox

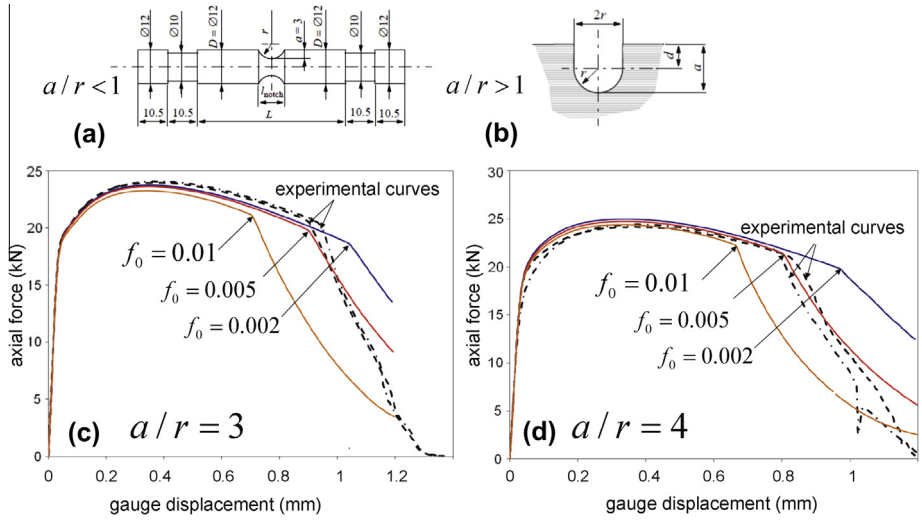

Fig. 6. Notched round bar tests used for calibrating the initial void volume fraction, f_0. Specimen geometry in mm: (A) $a/r < 1$ and (B) $a/r > 1$. Two tests for each of two notch geometries are shown along with simulations for several choices of f_0: (C) for $a/r = 3$ and (D) for $a/r = 4$.

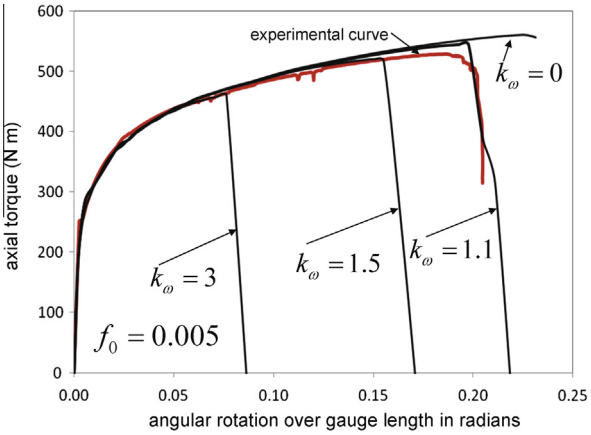

Fig. 7. Calibration of the shear damage coefficient, k_ω. Experimental data from the pure torsion test of the tension–torsion series of Part I compared with simulations of the specimen for four values of k_ω.

960 with base curve parameters given in Table 1 and $f_0 = 0.004$ and $k_\omega = 1$.

3.2. Simulation of the double-notched tension–torsion tests

The geometry of the double-notched specimen is shown in Fig 1(a)–(c) and Fig. A1(a) of Part I. The extended Gurson model has been implemented as user subroutines through the VUMAT interfaces in ABAQUS (2010). The Explicit version of this code has been used to carry out the simulations for the tension–torsion tests. The three dimensional finite element mesh used in the simulations of the tests is shown in Fig. 8. It is essential that a three dimensional model is used because generally the localization modes do not conform to axial symmetry, as seen in the fractographs in Fig. 10 of Part I. Eight-node linear brick elements with reduced Gaussian integration and hourglass control (C3D8R in ABAQUS Explicit) were used in all regions. Iterations on element size and meshing details were made prior to arriving at the mesh used to carry out the final analysis. As shown in Fig. 8, sufficiently refined mesh was used in the notch region; the smallest elements along the center line have dimensions about $50 \times 50 \times 250$ μm with 250 μm in the circumference direction. This mesh configuration is able to adequately capture near-axisymmetric deformation, and it is adequate for localizations with circumferential variations smaller than axial and through-thickness variations. The mesh would not accurately resolve shear localizations in which variations in the circumferential direction are relatively large.

Outside the notch region, the mesh was gradually coarsened in the length direction. The elemental size in the circumference direction was kept as 250 μm. The loading, same as what described in Part I, was applied to both ends of the specimen simultaneously. For precisely controlling the ratio of the axial force and the torque, a user subroutine through the VUAMP interface in ABAQUS Explicit was utilized, where the calculated axial load from the previous step was monitored at the beginning of each step and then the applied torque is updated at the end of the current step according to the prescription.

The reader is referred to the details of the test protocol which are laid out in Section 2.1 of Part I. The numerical simulations attempted to reproduce these details to the full extent possible. With F as the axial force and M as the torque applied to the specimen, each test was conducted under proportional loading with $\kappa = FR_m/M$ maintained constant, with R_m as the radius to the middle of the notch of the undeformed specimen. Note that this ratio is equivalent to the ratio of the true axial and shear stresses averaged over the plane at the center of the notch, $\kappa = \overline{\sigma}_{axial}/\overline{\tau}_{shear}$. For presenting data, the relative proportion of axial stress to shear stress is measured by

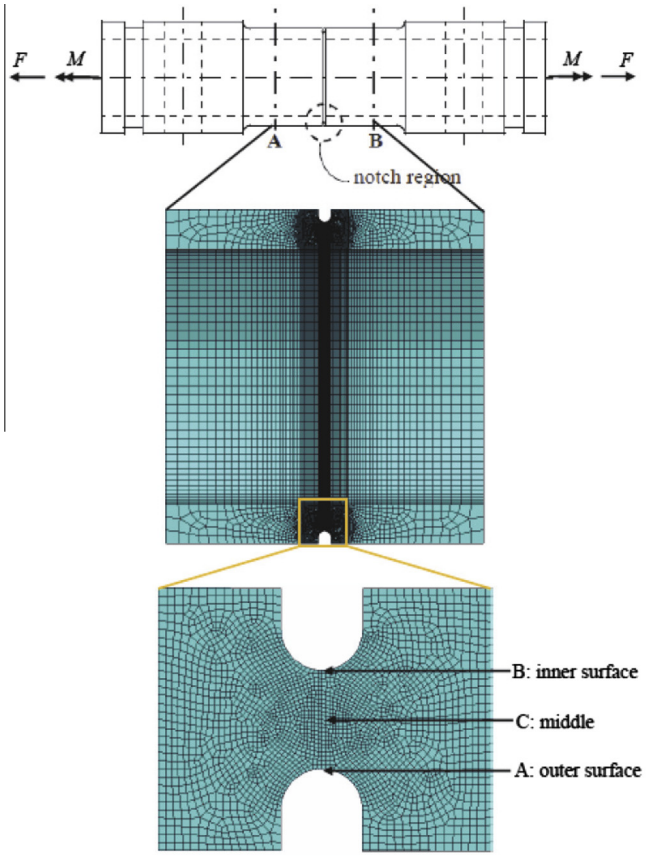

Fig. 8. The tension–torsion specimen and the finite element mesh used in the finite element analysis.

$$k_T = \frac{\kappa}{\kappa + 1} = \frac{\overline{\sigma}_{axial}}{\overline{\sigma}_{axial} + \overline{\tau}_{shear}} \tag{14}$$

ranging from 0 in pure torsion to 1 in pure axial force. Results from the calculations will be presented for the equivalent plastic strain at failure at several points throughout the neck. In addition, the definition given in Section 3.1 of Part I of an "overall equivalent plastic strain" expressed in terms of the normal displacement across the notch, δ_n, and the rotation across the notch, θ_n, will also be used because it allows direct comparison with quantities measured in the tests.

The simulations are carried out using the extended Gurson model with constitutive inputs for Weldox 420 and 960 as described above. In the simulations, the actual dimensions of the specimen have been used. To facilitate comparison with the experimental data, some of the results will be presented in dimensional form. It is useful to begin with the simulations of the overall load–displacement behavior for Weldox 420 presented in Fig. 9. Curves for torque versus rotation across the notch and axial force versus displacement across the notch are plotted for the full range of simulations with k_T prescribed to be constant in each case. The curves in Fig. 9 were not computed with precisely the same values of k_T for the individual tests of Part I, but Fig. 10 shows direct comparisons of the simulations and the experiments for two of the tests. The simulations are of the quantities directly measured in the experiments. In this paper, the onset of the abrupt down-turn in the load–displacement curves seen in Figs. 9 and 10 is identified

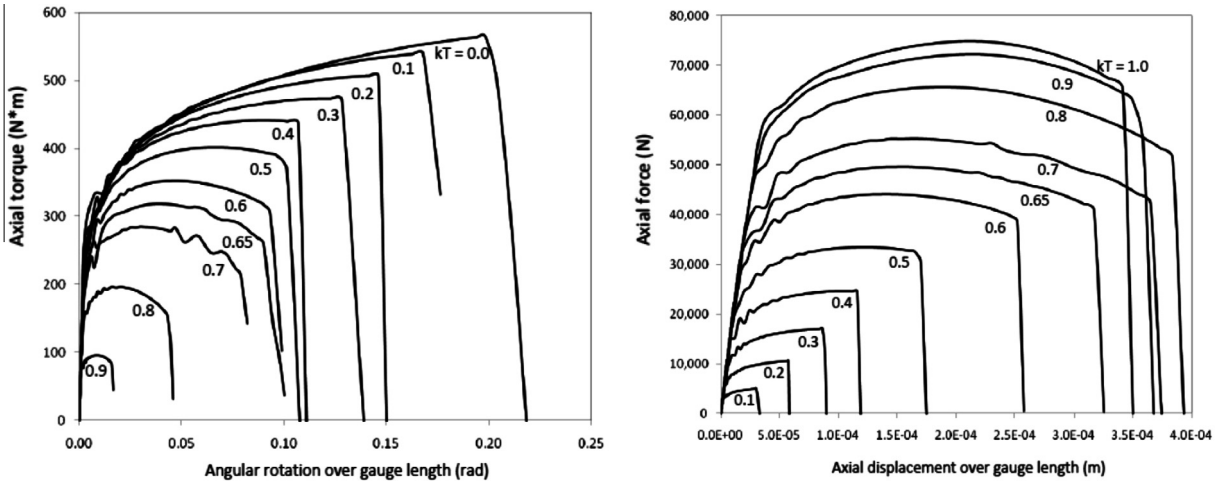

Fig. 9. Computed curves of torque versus rotation across the notch and axial force versus axial displacement across the notch for the series of tests, each with constant k_T, for Weldox 420.

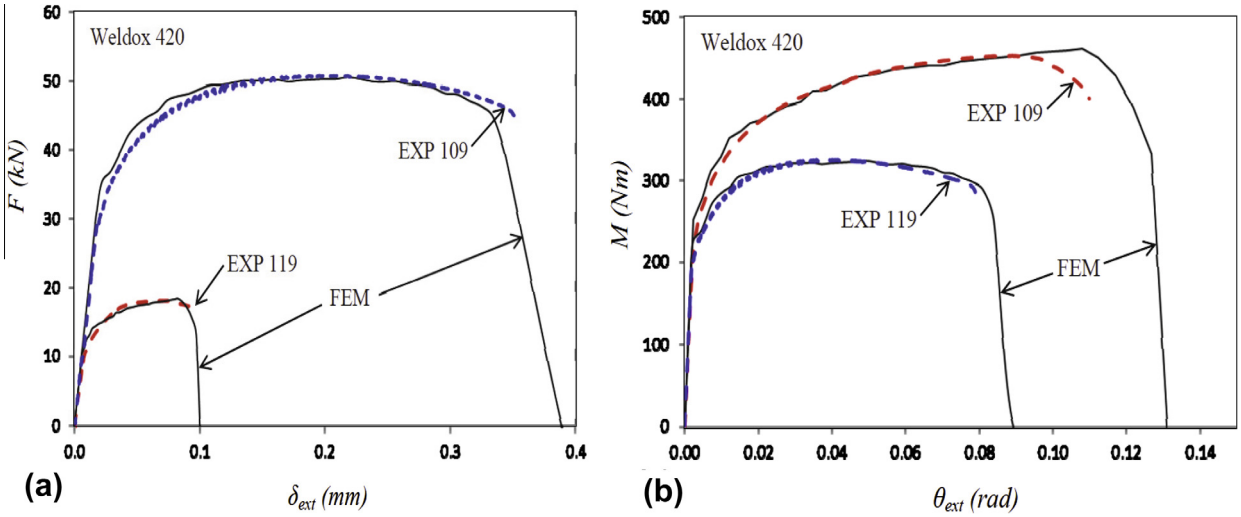

Fig. 10. Comparison of simulations with experimentally measured force–displacement relation in (a) and moment-twist relation in (b) for two of the experiments. Experiment 109 has $k_T = 0.324$ and experiment 119 has $k_T = 0.651$.

as the point of failure, and the equivalent plastic strain associated with this point is labeled the fracture strain. The down-turn point is associated with some combination of a shear or normal localization spreading across the notch, as will be discussed below. Thus, the definition of the fracture strain is tied to formation of the band of localization, consistent with the definition in Section 2. Local strains larger than this fracture strain will occur within the localization band itself, but for the purposes of characterizing the tests, as well as for engineering applications, a definition of fracture strain based on the onset of an abrupt loss of strength is the proper choice. Further discussion related to the identification of the fracture strain will be given later.

Fig. 11 presents the overall equivalent plastic strain at fracture as measured in the test series for Weldox 420 and the predicted results based on the calibrated damage parameters ($f_0 = 0.005$, $k_\omega = 1.1$), as well as results predicted for two other choices of damage parameters. The results based on the calibrated constitutive parameters reproduce the experimental trend reasonably well. In particular, they capture the non-monotonic trend with increasing k_T and the local peak in fracture strain at $k_T \cong 0.65$. The stress state in the notch varies from essentially pure shear ($\omega = 1$) at $k_T = 0$, to an axisymmetric state (uniaxial stress plus hydrostatic tension with $\omega = 0$) at $k_T \cong 0.7$, to plane strain tension with superimposed hydrostatic tension at the center of the notch ($\omega \cong 1$) at $k_T = 1$. The dependence of ω in the notch on k_T is very similar to that plotted for the model problem in Fig. 4. As noted in connection with the model problem in Section 2.2, the Gurson model without the extension ($k_\omega = 0$) would not predict a local peak in the fracture strain. Moreover, if f_0 were chosen such that the predictions gave a reasonable fit for the data at $k_T = 1$, then the fracture strain predicted for k_T less than about 0.3 would be unrealistically large.

Two additional curves in Fig. 11 have been included to illustrate the sensitivity of the predictions to the choice of the damage parameters. With $f_0 = 0.002$ and $k_\omega = 1.5$, the experimental data for pure torsion and pure axial extension (both with $\omega \cong 1$) is well predicted, but for k_T in the mid-range the prediction significantly overestimates experimental data because the initial void volume fraction is too small. Conversely, with $f_0 = 0.005$ and $k_\omega = 1.5$, the predictions fit the experimental data fairly well for $k_T \geqslant 0.3$, but significantly underestimate the experimentally measured shear strain at fracture in pure torsion because the shear damage coefficient is too large.

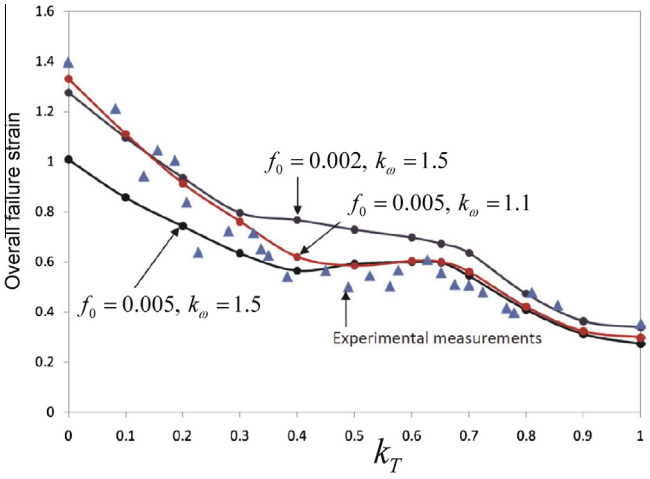

Fig. 11. A comparison of the experimental data for the tension–torsion tests for Weldox 420 with finite element simulation based the extended Gurson model. The overall plastic strain at fracture (defined in Part I) versus the relative proportion of tension to torsion as measured by k_T. The calibrated damage parameters for Weldox 420 are ($f_0 = 0.005,\ k_\omega = 1.1$). Predictions for two other sets of damage parameters are show to give an indication of the sensitivity to these parameters.

The stresses and strains are not uniformly distributed across the notch as has been emphasized in Part I. The equivalent plastic strain has a minimum at the center of the notch when k_T is small and shear bands emerge from the edges of the notch and spread towards the center. The distribution of the effective void volume fraction, f, across the notch within the shear band at the onset of fracture is shown in Fig. 12 for three loading cases, $k_T = 0$, 0.7 and 1 as simulated by the extended Gurson model for Weldox 420. For torsional loading, $k_T = 0$, the stress concentration at the edges of the notch promotes the emergence of the shear band, while for the other two loadings, $k_T = 0.7$ and 1, the higher triaxiality at the middle of the notch accelerates void grow and triggers the onset of the shear band at that location.

Further insight into the non-uniform behavior in the notch is displayed in Fig. 13 where the equivalent plastic strain at the edges and middle of the notch are plotted as a function of the overall equivalent plastic strain for Weldox 420 for pure torsional loading. Strains within the incipient shear band are compared with those

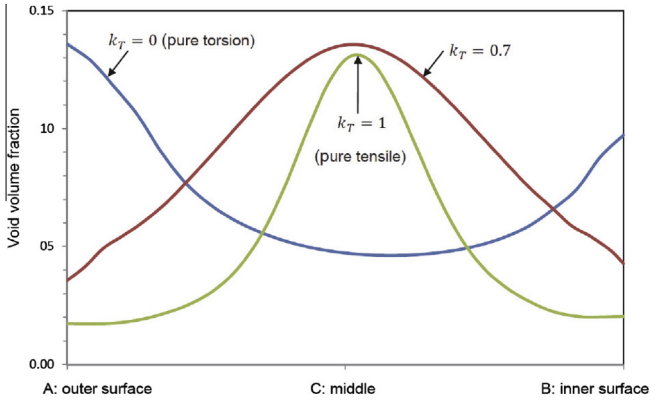

Fig. 12. Distribution of the effective void volume fraction across the notch midplane within the shear band just at the onset of the abrupt down-turn of the overall load–deflection behavior for Weldox 420 for three loadings: $k_T = 0$ (torsion), $k_T = 0.7$ and $k_T = 1$ (tension). For the torsional loading, $k_T = 0$, shear localization starts at the edges of the notch and propagates inward. For the other two loadings, the shear band first forms in the middle of the notch where the triaxiality is the highest and then spreads outward towards the edges.

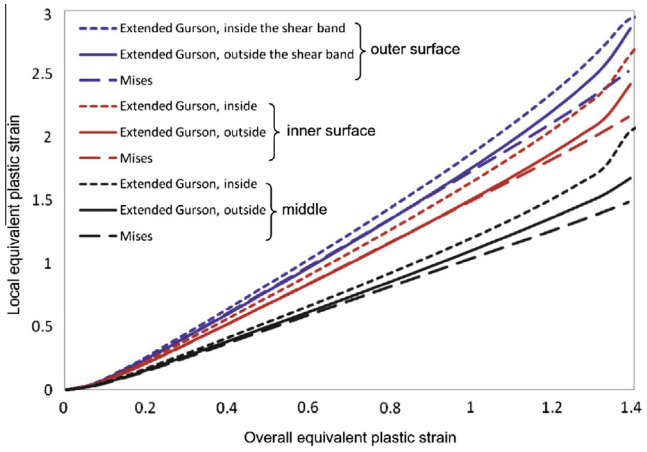

Fig. 13. The equivalent plastic strain at three locations within the minimum section of the notch as a function of the overall equivalent plastic strain for Weldox 420 for torsional loading ($k_T = 0$). As noted in Fig. 12, for this loading the strains are larger at the outer and inner surfaces than at the middle of the notch. Three predictions are shown for each location: (1) based on Mises theory with no damage (i.e., $f_0 = 0$) using precisely the same mesh, based on the extended Gurson model *within the incipient shear band* (2), and *just outside the incipient shear band* (3). The strains within and outside the emerging shear band begin to diverge prior to the onset of failure in torsion at overall equivalent plastic strain slightly less than 1.4. The results for Mises plasticity with no damage are reasonably accurate until the overall strain approaches the onset of failure.

just outside the band as predicted using the extended Gurson model. As the onset of fracture is approached the strains within the band begin to increase more rapidly than those just outside the band, as is especially noticeable in the middle of the notch. Also included in Fig. 13 is the prediction at the three locations based on Mises theory with no damage (i.e., the present constitutive model with $f_0 = 0$) using precisely the same mesh. The predictions with no damage are accurate until a point just prior to the onset of fracture when the extended Gurson model predicts significant shear band localization. These findings validate the use of the classical Mises theory in Part I to establish the strain distributions associated with the experimentally measured onset of fracture.

As noted above, the simulations of the tension–torsion specimen reveal that shear localization starts either at the edges of the notch or at the center and spreads across the entire notch cross section. For example, the abrupt downturn in the torque-twist behavior seen in Fig. 7, and the down-turn for all the curves in Fig. 9, does not occur until the shear band has spread across the entire central plane of the notch. Thus, the definition of "fracture" employed here is not associated with the first formation of a localization band. Instead, fracture is taken as the point where the localization spreads across the structural element causing a drop in load carrying capability. One must be cognizant of such considerations when invoking the concept of a critical plastic strain to characterize ductile fracture in structural applications. The fact that simulations in Fig. 13 based on Mises plasticity with no damage agree reasonably closely to those based on the extended Gurson model prior to fracture underpins the use of an engineering fracture criterion based on a critical plastic strain computed using Mises plasticity.

The details of the results for Weldox 960 are similar to those discussed above and, thus, only the comparison between the experimental and numerically simulated results for the overall equivalent plastic strain at fracture is presented in Fig. 14. As in the case of the intermediate strength steel, the simulations based on the extended Gurson model capture the experimental trend rather well. The fracture strains of Weldox 960 are about one half of those of Weldox 420 as expected given that the strength of the

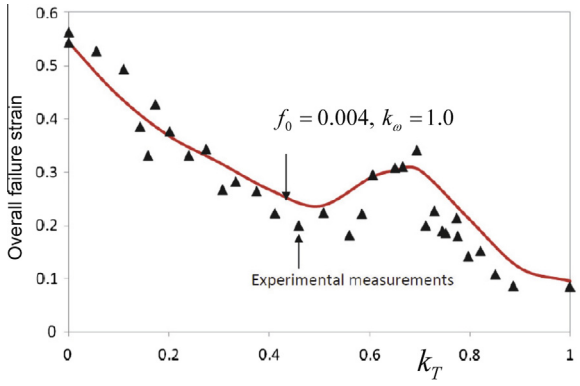

Fig. 14. A comparison of the experimental data for the tension–torsion tests for the high strength steel Weldox 960 with finite element simulation based the extended Gurson model. The overall plastic strain at fracture (defined in Part I) versus the relative proportion of tension to torsion as measured by k_T.

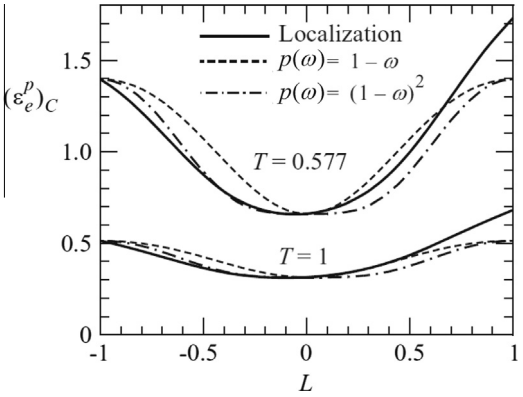

Fig. 15. Effective plastic strain at the onset of shear localization as dependent on the full range of the Lode parameter, L, for two levels of triaxiality computed using the extended Gurson model with the material parameters for Weldox 420 specified in Section 2.2. Included are the plots of the proposed extension to the phenomenological fracture strain criterion (15) based on the linear ($p(\omega) = 1-\omega$) and quadratic ($p(\omega) = (1-\omega)^2$) interpolation functions chosen to reproduce axisymmetric stress states with $L = -1$ ($\omega = 0$) and shearing stress states with $L = 0$ ($\omega = 1$).

former is about twice that of the latter. The damage parameters for Weldox 960 ($f_0 = 0.004$, $k_\omega = 1$) are not too different from those for Weldox 420 ($f_0 = 0.005$, $k_\omega = 1.1$), but the lower straining hardening ($N = 0.059$ versus $N = 0.18$) and higher initial yield stress ($\sigma_Y = 996$ MPa versus $\sigma_Y = 415$ MPa) are also important in determining localization.

4. An extension of the Hancock–Mackenzie/Johnson–Cook criterion for ductile fracture

Motivated by the experimental results in the previous section and the localization predictions based on the extended Gurson model in Section 2, we propose a phenomenological ductile fracture criterion for initially isotropic metal alloys based on a critical effective plastic strain suitable for engineering applications. The proposal incorporates a dependence of the effective plastic strain at fracture on stress triaxiality, $T = \sigma_m/\sigma_e$, as in the criterion of Hancock and Mackenzie (1976) and Johnson and Cook (1985), as well as on the invariant measure ω defined in (2) which discriminates between axisymmetric states and shearing states. It has been noted earlier that the difference between fracture in states with different signs of the Lode parameter, such as between axisymmetric states with $L = \pm 1$, is relatively small compared to the difference between axisymmetric states and shearing states. This assertion is supported by the present simulations and those of Nahshon and Hutchinson (2008) and Barsoum and Faleskog (2011). The dependence on the sign of the Lode parameter will be neglected in the criterion given below by assuming a dependence on ω, but not on the sign of L. This issue will be discussed further later in this section.

Denote the effective plastic strain at fracture as a function of triaxiality, T, and ω by $\varepsilon(T,\omega)$. Denote the limit for axisymmetric states ($L = \pm 1$, $\omega = 0$) by $\varepsilon_A(T) = \varepsilon(T,0)$ and the limit for shearing states ($\omega = 1$) by $\varepsilon_S(T) = \varepsilon(T,1)$. The simulations in Section 2 indicate that at any T, $\varepsilon_A(T)$ is the upper limit and $\varepsilon_S(T)$ is the lower limit. If fracture strains for these two limits were known, an interpolation of these two limiting states can be expressed as

$$\varepsilon(T,\omega) = (1 - p(\omega))\varepsilon_S(T) + p(\omega)\varepsilon_A(T) \tag{15}$$

with $p(0) = 1$ and $p(1) = 0$. Shear localization calculations for Weldox 420 will be used to guide the choice of the interpolation function $p(\omega)$.

Fig. 15 presents curves of effective plastic strain at the onset of shear localization computed for Weldox 420 over the full range of the Lode parameter for two levels of stress triaxiality. These results have been computed using the formulation described in Section 2.2 wherein the principal stresses, ($\sigma_I, \sigma_{II}, \sigma_{III}$), are increased proportionally with fixed T and L. As noted earlier, the localization strain for Case II ($L = 1$) is slightly larger than that for Case I ($L = -1$) at the same triaxiality. The prediction of (15) for two possible interpolation functions is included in Fig. 15: a linear interpolation with $p(\omega) = 1 - \omega$ and a quadratic interpolation with $p(\omega) = (1-\omega)^2$. Of the two, the quadratic interpolation is clearly superior, and, given its simplicity, it will be used in the sequel, although other interpolation functions could be considered.

The following implementation of the phenomenological fracture relation (15) illustrates its potential in practical applications. The illustration will apply (15) to the tension–torsion "data" in Fig. 3 using the results on axisymmetric and shear states presented for the same material in Fig. 2. In this scheme, four experimental data points are used to calibrate the relation. Take $\varepsilon_A(T) = b_A e^{-c_A T}$ and determine b_A and c_A by fitting to axisymmetric data for two triaxiality levels (illustrated here using $T = 1/3$, and $T = 1/\sqrt{3}$ with $L = -1$ ($\omega = 0$) from Fig. 2). Then, with $\varepsilon_S(T) = b_S e^{-c_S T}$, determine b_S and c_S by fitting to data for shearing stress states ($\omega = 1$) at two triaxiality levels (here using pure shear, $T = 0$, and plane strain tension, $T = 1/\sqrt{3}$ from Fig. 2). This calibration procedure yields

$$\varepsilon_C(T,\omega) = [1 - p(\omega)]1.6e^{-1.97T} + p(\omega)9.07e^{-4.25T}. \tag{16}$$

Based on the expressions for T and ω in (12), the fracture strain from (16) with $p(\omega) = (1-\omega)^2$ is plotted in Fig. 3. The phenomenological relation does a reasonably good job of reproducing the extended model predictions in Fig. 3 over the entire range of the simplified tension–torsion test. A plot illustrating the role of the two bounding curves in (15), the upper limit for axisymmetric states and the lower limit for shearing states, is presented in Fig. 16, with the schematic trend of the torsion-tension tests imposed.

One difficulty in establishing any phenomenological critical plastic fracture criterion, including the present, is that experimental data for axisymmetric states at low triaxiality, i.e., $\varepsilon_A(T)$ for $T < 0.3$, requires high pressure test procedures such as those conducted by Bridgman (1953). The effective plastic strain to fracture in shearing states, $\varepsilon_S(T)$, can be measured experimentally at lower triaxiality more readily than $\varepsilon_A(T)$ (Mohr and Ebnoether, 2009). Moreover, based on the present study, it might be argued that $\varepsilon_S(T)$ is the more fundamental of the two limits in that $\varepsilon_S(T)$ provides the lower limit on the fracture strain at a given triaxiality.

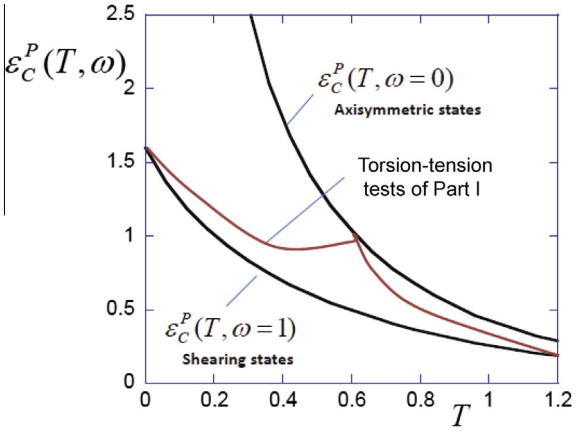

Fig. 16. A schematic plot illustrating the phenomenological critical strain criterion (15) showing the two bounding curves: the upper curve for axisymmetric stress states and the lower curve for shearing stress states. The schematic trend of the torsion-tension tests between these two limiting curves is also included.

This section concludes with further discussion of the possible importance of the sign of the Lode parameter, and, specifically, the evidence for a difference in fracture strain at the same triaxiality between axisymmetric states with $L=-1$, Case I, (with $\sigma_I > \sigma_{II} = \sigma_{III}$) and $L=1$, Case II, (with $\sigma_I = \sigma_{II} > \sigma_{III}$). Shear band localization results in Figs. 1 and 2 based on the Gurson model, as well as the results in Fig. 15, indicate that Case II has a slightly larger effective strain at localization than Case I at all triaxialities. This trend is also seen in Fig. 17 where the role of the strain hardening exponent on the Lode parameter dependence of the localization strain is brought out. At low strain hardening, asymmetry with respect to L is somewhat more pronounced than at higher strain hardening, implying that the symmetric model (15) will be less accurate at low hardening. Nevertheless, the dominant effect remains the distinction between shearing states ($\omega=1$) and axisymmetric states ($\omega=0$), particularly at lower and intermediate triaxialies. The localization study of Barsoum and Faleskog (2011), based on three-dimensional void simulations, also confirms these trends.

Bai and Wierzbicki (2008) assert that a large difference in fracture strain may exist between the axisymmetric Cases I and II (e.g., see their Fig. 14). Moreover, they suggest that the strain associated with Case II is significantly less than that for Case I, in stark contrast to the trends noted here. They base their argument on fracture strains measured in an upsetting test – a squat cylindrical specimen subject to compression that develops a barrel shape with tensile circumferential stresses at the surface and tensile radial stresses at the center. Bai and Wierzbicki view the upsetting test as an example of Case II ($\sigma_I = \sigma_{II} > \sigma_{III}$), which is the correct characterization of the stress state along the central axis of the specimen. However, fracture occurs at the surface of the specimen due to the barreling, not at its center. The surface is in a state of plane stress. Thus, for example, an upsetting test having zero triaxiality at its surface has $\sigma_{III} = -\sigma_I$, $\sigma_{II} = 0$ corresponding to a state of pure shear ($L=0,\ \omega=1$). In such cases, the shear crack is observed to form with its plane normal to the surface at roughly 45° to the axis of the specimen in accord with what would be expected for a shear localization evolving into a shear crack.

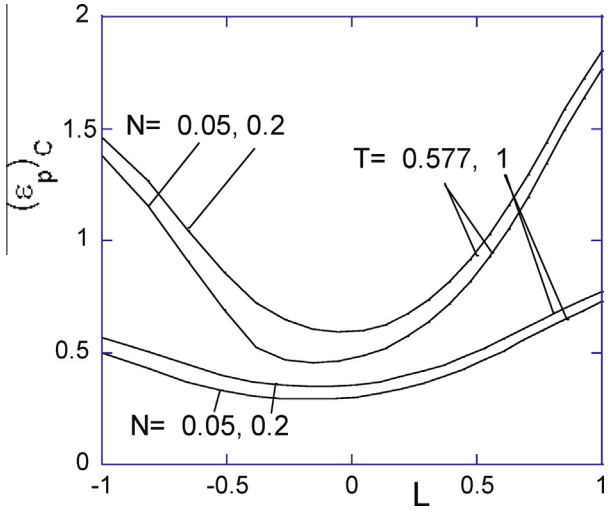

Fig. 17. The effect of the strain hardening exponent on the Lode parameter dependence of the localization strain for two levels of triaxiality based on the computational model in Section 3. Apart from the strain hardening exponent, N, the parameters are the same as those in Fig. 15.

Several recent publications have taken steps to address the limitations of the Johnson–Cook fracture criterion based solely on triaxiality. A modification of the Johnson–Cook criterion introducing a dependence on the Lode parameter has been given by Chocron et al. (2011) with emphasis on ballistic applications. Details of the Chocron et al. modification differ from the present proposal (15), but their proposal also neglects dependence of the sign of the Lode parameter, consistent with the assertions made here. Kane et al. (2011) consider a ductile fracture criterion for application in the range of low triaxiality with a dependence on the Lode parameter. Their criterion incorporates a difference between the axisymmetric Cases I and II that is in accord with the trend of the present results, i.e., with the fracture strain in Case II being somewhat larger than that in Case I. However, the criterion of these authors does not incorporate the significant reduction in fracture strains for shearing states relative to axisymmetric states seen in the experimental data in Part I for Weldox 420 and 960 and in the data for Al 2024-T351 of Bao and Wierzbicki (2004). Lou et al. (2012) have proposed a criterion for the critical plastic strain for plane stress states with applications to sheet metal forming limits and have compared their criterion with data from an extensive series of sheet metal tests. Their criterion incorporates a dependence on the Lode parameter which produces non-monotonic trends on triaxiality similar in many respects to those that emerge here. Finally, it can be noted that Gruben et al. (2011) have conducted fracture tests on a series of dual phase steel specimens at different combinations of triaxiality and Lode parameter. Their data also reveals an increase in the effective plastic strain under increasing triaxiality at axisymmetric stressing associated with uniaxial tension, with trends qualitatively similar to that of the Weldox steels but with less variation in the critical plastic strain.

5. Conclusions

The two damage parameters of the extended Gurson model, f_0 and k_ω, have been calibrated for two steels, Weldox 420 and 960, using a combination of notched round bar and shear tests. The calibrated model has then been used in a finite element code to simulate the fracture strains in the tension–torsion test series of the two steels reported in Part I. The simulations reproduce the main features of the test series with reasonable fidelity. In particular, they capture the fact that the fracture strain does not decrease monotonically with increasing stress triaxiality. The essence of the extended Gurson model that makes it possible to reproduce the experimental trend is the incorporation of damage growth in shear through a dependence on the parameter ω defined in (2) which discriminates between axisymmetric and shearing stress states.

The Gurson model and its extension have been derived and validated under proportional, or near-proportional, stressing and straining conditions. Thus, it should not be expected that the constitutive model used here would be able to capture the growth of void damage under loading histories that are distinctly non-proportional, as for example if the present specimens were first deformed in tension well into the plastic range and then subject to failure in torsion. The development of constitutive relations capable of capturing the strong history-dependence of ductile fracture remains an open challenge. Similarly, the phenomenological critical plastic strain criterion (15) should not be expected to be valid under strongly non-proportional conditions.

The definition of a fracture strain for engineering purposes is not straightforward. For the test specimens, the definition adopted in Part I and followed here employs a measure of the overall effective plastic strain in the notch at the point where an abrupt downturn in the load carrying capacity begins. The simulations show that this downturn occurs when the shear localization has first spread across the entire width of the notch. The beginning of the fracture process is the onset of shear localization at a local point within the notch. The fracture strain defined here occurs slightly later in the process but still prior to crack initiation.

Recent experimental work has convincingly shown that the third stress invariant must be taken into account in addition to stress triaxiality in criteria for fracture of nominally isotropic ductile alloys. A modification of the critical effective plastic strain criterion of Hancock and Mackenzie (1976) and Johnson and Cook (1985) has been suggested in Section 4. As the measure of the third stress invariant, this modification employs ω which distinguishes between axisymmetric and shearing stress states. The brief review of recent literature in Section 4 highlights the fact that there are a number of open issues related to how the third stress invariant should be brought into any modification, e.g., through the Lode parameter or through the more restrictive parameter ω. The shear localization study carried out in Section 2 suggests that the dependence on the sign of the Lode parameter is relatively small compared to the difference between axisymmetric and shearing states, as suggested earlier by the more fundamental study of Barsoum and Faleskog (2011). These studies show that shear localizations occur in Case I ($\sigma_I > \sigma_{II} = \sigma_{III}$) at only slightly lower strain than in Case II ($\sigma_I = \sigma_{II} > \sigma_{III}$). Given this finding and the lack of experimental data presently available to discriminate between these two types of axisymmetric states, the criterion proposed in Section 4 neglects the influence of the sign of the Lode parameter by employing the measure ω. The multi-axial extension of the Johnson–Cook fracture criterion (15), as illustrated in Fig. 16, has a relatively simple form which exploits the assertion that, at any triaxiality, axisymmetric states have the highest fracture strain and shearing states have the lowest. It remains for future work to clarify some of the issues highlighted above concerning the manner in which the third stress invariant is brought into the modified dependence.

Acknowledgment

The work of JWH was supported in part by the Office of Naval Research (N00014-07-0764) and in part by Harvard University.

References

ABAQUS, 2010. User's Manual Version 6.10, Dassault Systemes.
Bai, Y., Wierzbicki, T., 2008. A new model of metal plasticity and fracture with pressure and Lode dependence. Int. J. Plast. 24, 1071–1096.
Bao, Y., Wierzbicki, T., 2004. On fracture locus in the equivalent strain and stress triaxiality space. Int. J. Mech. Sci. 46, 81–98.
Barsoum, I., Faleskog, J., 2011. Micromechanical analysis on the influence of the Lode parameter on void growth and coalescence. Int. J. Solids Struct. 48, 925–938.
Bridgman, P.W., 1953. The effect of pressure on the tensile properties of several metals and other materials. J. Appl. Phys. 24, 560–570.
Chocron, S., Eirce, B., Anderson, C.E., 2011. A new plasticity and failure model for ballistic application. I. J. Impact Eng. 38, 755–764.
Faleskog, J., Barsoum, I., 2013. Tension–torsion fracture experiments – Part I: Experiments and an evaluation procedure for the effective plastic strain (Part I of the present paper – to be published).
Faleskog, J., Gao, X., Shih, C.F., 1998. Cell model for nonlinear fracture analysis – I. Micromechanics calibration. Int. J. Fract. 89, 355–373.
Gruben, G., Fagerholt, E., Hopperstad, O.S., Borvik, T., 2011. Fracture characteristics of a cold-rolled dual-phase steel. Eur. J. Mech. A/Solids 30, 204–208.
Gurson, A.L., 1977. Continuum theory of ductile rupture by void nucleation and growth – Part I. Yield criteria and flow rules for porous ductile media. J. Eng. Mater. Technol. 99, 2–15.
Haltom, S.S., Kyriakides, S., Ravi-Chandan, I.K., 2013. Ductile failure under combined shear and tension. Int. J. Solids Struct. 50, 1507–1522.
Hancock, J.W., Mackenzie, A.C., 1976. On the mechanisms of ductile fracture in high-strength steels subject to multi-axial stress states. J. Mech. Phys. Solids 24, 147–160.
Johnson, G.R., Cook, W.H., 1985. Fracture characteristics of three metals subject to various strains, strain rates, temperatures and pressures. Eng. Fract. Mech. 21, 31–48.
Kane, A., Borvik, T., Berstad, T., Benallal, A., Hopperstad, O.S., 2011. Failure criteria with unilaterial conditions for simulation of plate perforation. Eur. J. Mech. A/Solids 30, 468–476.
Kim, J., Gao, X., Srivatsan, T.S., 2004. Modeling of void growth in ductile solids: effects of stress triaxiality and initial porosity. Eng. Fract. Mech. 71, 379–400.
Lou, Y., Huh, H., Lim, S., Pack, K., 2012. New ductile fracture criterion for prediction of fracture forming limit diagrams of sheet metals. Int. J. Solids Struct. 49, 3605–3616.
Marciniak, K., Kuczynski, K., 1967. Limit strains in the process of stretch forming sheet metal. Int. J. Mech. Sci. 9, 609–620.
Mohr, D., Ebnoether, F., 2009. Plasticity and fracture of martensitic boron steel under plane stress conditions. Int. J. Solids Struct. 46, 3535–3547.
Nahshon, K., Hutchinson, J.W., 2008. Modification of the Gurson model for shear failure. Eur. J. Mech. A/Solids 27, 1–17.
Scheyvaerts, F., Onck, P.R., Tekoglu, C., Pardoen, T., 2010. The growth and coalescence of ellipsoidal voids in plane strain under combined shear and tension. J. Mech. Phys. Solids 59, 373–397.
Tvergaard, V., 2008. Shear deformation of voids in a shear field. Int. J. Mech. Sci. 50, 1459–1465.
Tvergaard, V., 2009. Behavior of voids in a shear field. Int. J. Fract. 158, 41–49.
Tvergaard, V., Nielsen, K.L., 2010. Relations between a micro-mechanical model and a damage model for ductile failure in shear. J. Mech. Phys. Solids 58, 1243–1252.
Xue, L., Wierzbicki, T., 2008. Ductile fracture initiation and propagation modeling using damage plasticity theory. Eng. Fract. Mech. 75, 3276–3293.
Xue, Z., Pontin, M.G., Zok, F.W., Hutchinson, J.W., 2010. Calibration procedures for a computational model of ductile fracture. Eng. Fract. Mech. 77, 492–509.